

# Quantum oscillations from generic surface Fermi arcs and bulk chiral modes in Weyl semimetals

Yi Zhang<sup>1</sup>, Daniel Bulmash<sup>1</sup>, Pavan Hosur<sup>1</sup>, Andrew C. Potter<sup>2</sup>, and Ashvin Vishwanath<sup>2</sup>

<sup>1</sup> *Department of Physics, Stanford University, Stanford, California 94305, USA and*

<sup>2</sup> *Department of Physics, University of California, Berkeley, California 94720, USA.*

(Dated: December 22, 2015)

We re-examine the question of quantum oscillations from surface Fermi arcs and chiral modes in Weyl semimetals. By introducing two tools - semiclassical phase-space quantization and a numerical implementation of a layered construction of Weyl semimetals - we discover several important generalizations to previous conclusions that were implicitly tailored to the special case of identical Fermi arcs on top and bottom surfaces. We show that the phase-space quantization picture fixes an ambiguity in the previously utilized energy-time quantization approach and correctly reproduces the numerically calculated quantum oscillations for generic Weyl semimetals with distinctly curved Fermi arcs on the two surfaces. Based on these methods, we identify a ‘magic’ magnetic-field angle where quantum oscillations become independent of sample thickness, with striking experimental implications. We also analyze the stability of these quantum oscillations to disorder, and show that the high-field oscillations are expected to persist in samples whose thickness parametrically exceeds the quantum mean free path.

Weyl semimetals are three-dimensional quantum materials characterized by a band gap that closes at isolated points, Weyl nodes, in the Brillouin zone. Weyl nodes serve as sources of quantized monopole fluxes of  $\pm 2\pi$  Berry curvature, whose sign defines a chirality  $\chi = \pm 1$  for each node, and hence serves as an example of quantum topology in the absence of a band gap<sup>1,2</sup>. At a spatial surface, the bulk band topology produces unusual Fermi-arc surface states, whose Fermi “surface” consists of disjoint arc segments that pairwise connect surface projections of opposite chirality Weyl nodes<sup>1-4</sup>, and have been observed in photoemission experiments<sup>5,6</sup> and band-structure calculations<sup>7</sup> on crystalline materials. Moreover, in the presence of a magnetic field,  $\vec{B}$ , Weyl nodes exhibit chiral Landau level (LL) modes<sup>8</sup> with field-independent dispersion  $\varepsilon_{\chi,0} = \chi v_{\parallel} k_{\parallel}$ , where  $v_{\parallel}$ ,  $k_{\parallel}$  are respectively the velocity and momentum along  $\vec{B}$ .

Recently, it was shown<sup>9</sup> that an applied magnetic field perpendicular to the surface of a Weyl semimetal drives a novel kind of cyclotron orbit in which electrons slide along a Fermi-arc on the top surface from  $\chi = +1$  towards  $\chi = -1$  Weyl nodes, transfers to the bulk chiral LL mode of the  $\chi = -1$  node on which they propagate to the bottom surface, traverse the bottom Fermi-arc and return to the top surface via the mode with the opposite chirality. Ordinary cyclotron orbits around closed Fermi surfaces of metals are routinely studied via quantum oscillations, periodic-in- $1/B$  modulations in the density of states that appear in various thermodynamic and transport properties, and help unveil the detailed structure of the underlying Fermi surface. Ref. 9 showed that the quantized energy levels arising from these mixed surface and bulk cyclotron orbits indeed exhibit periodic quantum oscillations, whose phase exhibits a characteristic dependence on sample thickness that distinguishes them from conventional cyclotron orbits, and hence offering a direct probe of the topological connection between surface Fermi arcs and bulk Weyl bands. Experimental evi-

dence for such quantum oscillations was recently reported in the Dirac semimetal  $\text{Cd}_3\text{As}_2$ .<sup>10</sup> In addition, transport experiments were proposed based on the distinctive electronic properties of these cyclotron orbits<sup>11</sup>.

The semiclassical quantization of these cyclotron orbits in Ref. 9 was carried out through “energy-time” quantization, by demanding that the product of the energy,  $\varepsilon$ , of the electron and the semiclassical time of the orbit,  $t$ , equals an integer multiple of  $2\pi$ . Noting that  $t = (2L_z + 2k_0\ell_B^2)/v$ , where  $k_0$  is the  $k$ -space arc length of the Fermi arcs on the top and bottom surfaces,  $L_z$  is the sample thickness,  $v$  is the Fermi velocity, and  $\ell_B = 1/\sqrt{eB}$  is the magnetic length, the energy-time quantization condition states that the  $n^{\text{th}}$  quantized level crosses the chemical potential,  $\tilde{\mu}$  at field  $B = B_n$ :

$$\frac{1}{B_n} = \frac{e}{k_0} \left[ \frac{\pi v}{\tilde{\mu}} (n + \gamma) - L_z \right] \quad (1)$$

which occur periodically in  $1/B$  with period  $f = \frac{\pi e v}{k_0 \tilde{\mu}}$  and a thickness dependent phase offset:  $\phi(L_z) = 2\pi\gamma - \frac{2\tilde{\mu}L_z}{v}$ .

However, this approach leaves open a basic question: what is the overall zero of energy for  $\tilde{\mu}$ ? This issue is experimental pertinent, as it effects the frequency,  $f$ , of the quantum oscillations. We will show that the nature choice of the energy of the bulk Weyl node corresponds to the special case, implicitly assumed in Ref. 9, where the Fermi arcs on the top and bottom surfaces are identical. More generically, however, the Fermi arcs may have different shapes, and the zero of energy need not coincide with the Weyl node energy.

To generalize the results of Ref. 9 to include the generic case with arbitrarily curved Fermi arcs, we adopt an alternative phase-space quantization perspective in which the integral of momentum times spatial displacement is equal to  $\oint \vec{p} \cdot d\vec{r} = 2\pi(n + \gamma)$  for integer  $n$  and a constant quantum offset  $\gamma$ . Comparison to the energy-time quantization transparently identified the zero of energy

as where the surface arcs enclose zero  $k$ -space area using appropriate extrapolation from the chemical potential to lower energy. This method also predicts an additional thickness dependent correction to Eq. 1, which is difficult to obtain from the energy-time quantization perspective.

We next construct a tight-binding model based on a layered construction<sup>4</sup> of a Weyl semimetal, which enables the numerical simulation of Weyl semimetals with generic surface arcs. Using a recursive Greens function method, we numerically simulate the field dependence of the density of states in a magnetic field, and confirm the semiclassical predictions of the phase-space quantization scheme.

Finally, we discuss the experimental consequences of our results. First, we identify a special set of ‘magic’ angles of the magnetic field, for which the length-dependence of the phase of the quantum oscillations drops out. We explain how this effect enables a smoking gun signature of quantum oscillations from surface Fermi arcs in recently measured thin-film devices with non-parallel surfaces<sup>10</sup>. Second, we examine the effects of impurities, and find that these quantum oscillations are surprisingly resilient to disorder for sufficiently strong fields. In contrast to conventional quantum oscillations, which are obscured by disorder unless the cyclotron orbit is smaller than the quantum mean free path  $\ell_Q$ , we find that for strong fields, quantum oscillations from surface Fermi arcs and bulk chiral modes can persist in samples whose thickness substantially exceeds  $\ell_Q$ .

**Semiclassical phase-space quantization** – We begin by revisiting the semiclassical quantization of cyclotron orbits, which generically demands that the phase difference between successive Landau levels is equal to  $2\pi$ . The difference in phase accumulated between two successive levels for a fixed magnetic field can be expressed either in terms of the energy step and time or the difference in the product of momentum and displacement:

$$\Delta\phi = \int \Delta\varepsilon dt = \int \frac{\Delta\varepsilon}{v_F} dr = \Delta \oint \vec{p} \cdot d\vec{r} = 2\pi \quad (2)$$

where  $v_F = \frac{\partial\varepsilon}{\partial p_\perp}$  is the Fermi velocity,  $p_\perp$  is the momentum perpendicular to the orbit, and the last integral is over the spatial trajectory of the semiclassical orbit. For a simple derivation via path integral, see Appendix A. Importantly, Eq. 2 is expressed through the difference in energy of neighboring Landau levels but makes no reference to their absolute position. While the overall energy scale is unimportant for, e.g. spectroscopy which probes only energy differences, quantum oscillations experiments are conducted by varying  $B$  at fixed chemical potential  $\mu$ , such that the periodicity of quantum oscillations depends explicitly on the “zero of energy”.

Alternatively, the phase-space quantization framework offers an unambiguous reference to the energy, in which the momentum-displacement is integrated along the cyclotron orbit of constant energy contour at a specific chemical potential. In Appendix B, we show how to rec-

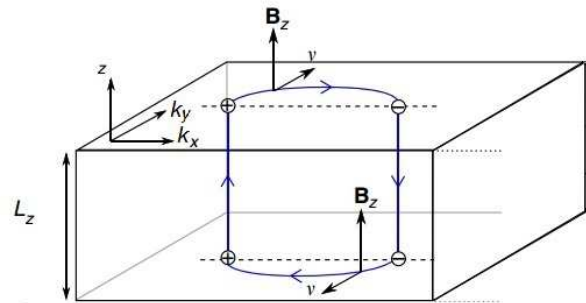


FIG. 1: Schematic plot of a semiclassical orbit of a Weyl semimetal slab in a perpendicular magnetic field. The electrons traverse the Fermi arc on the top surface, travel through the one-dimensional chiral mode parallel to the magnetic field in the bulk, traverse the corresponding Fermi arc on the bottom surface, and then return along the opposite chiral mode through the bulk. Note that the real-space orbit in the  $x-y$  plane is rotated by  $90^\circ$ .

oncile these methods, however, in the mean time we proceed with the more transparent phase-space quantization approach.

For the semiclassical cyclotron orbits described in Ref. 9, the phase-space quantization condition is  $\oint \vec{p} \cdot d\vec{r} = \oint \vec{k} \cdot d\vec{r} - e \oint \vec{A} \cdot d\vec{r} = 2\pi(n + \gamma)$ , where the integral is over the four segments of the orbit: two Fermi arcs on the surfaces and two chiral modes in the bulk parallel to the magnetic field<sup>17</sup>, as illustrated in Fig. 1. Throughout, we choose the convention that chemical potential,  $\mu$ , is measured from the energy of the Weyl nodes in the bulk.

For the Fermi arcs,  $\int \vec{p} \cdot d\vec{r} = e\Phi_z$ , where  $\Phi_z$  is the magnetic flux contained within the real-space orbit of area  $S_R$  in the  $x-y$  plane<sup>12</sup>. The semiclassical equations of motion imply

$$\Phi_z = B_z S_R = B_z S_k \ell_B^4 = \frac{S_k}{e^2 B_z} \quad (3)$$

where  $S_k$  is the  $k$ -space area enclosed by the two Fermi arcs combined and  $B_z$  is the  $\hat{z}$  component of the magnetic field  $\vec{B}$ . On the other hand, the chiral modes in the bulk are parallel to the magnetic field, so  $\int \vec{A} \cdot d\vec{r} = 0$  and:

$$\int \vec{p} \cdot d\vec{r} = \int \vec{k} \cdot d\vec{r} = L_z \sec \theta \left( \vec{k}_W \cdot \hat{B} + 2 \frac{\mu}{v_\parallel} \right) \quad (4)$$

where  $\theta$  is the tilting angle of  $\vec{B}$  from the surface normal,  $\vec{k}_W$  is the wave vector from + to - chirality Weyl nodes, and  $\pm \frac{\mu}{v_\parallel}$  are the Fermi wave vectors of their respective chiral modes with velocity  $v_\parallel$  parallel to  $\vec{B}$ , at chemical potential  $\mu$ . Adding the contributions, phase-space quantization implies that quantum oscillations occur at fields:

$$\frac{1}{B_n} = \frac{e}{S_k} \left[ 2\pi(n + \gamma) \cos \theta - L_z \left( \vec{k}_W \cdot \hat{B} + \frac{2\mu}{v_\parallel} \right) \right] \quad (5)$$

Eq. 5 is the main result of this paper.

When  $\mu$  is close to the Weyl nodes and the Fermi velocity  $v_s$  is approximately constant along the surface Fermi arcs, we can expand  $S_k = S_{k,0} + k_0^T \mu / v_s$ , where  $S_{k,0}$  and  $k_0^T$  are the enclosed  $k$ -space area and total length of the combination of the two Fermi arcs from both surfaces for  $\mu$  at the Weyl nodes. The frequency of the quantum oscillations  $f = 1/\Delta(\frac{1}{B})$  is

$$\begin{aligned} f &= S_k / 2\pi e = (S_{k,0} + k_0^T \mu / v_s) / 2\pi e \\ &= k_0^T (\mu_0 + \mu) / 2\pi e v_s \end{aligned} \quad (6)$$

where  $\mu_0 = S_{k,0} v_s / k_0^T$ . We see that our results reduce to those of Ref. 9, under the special conditions:  $S_k(\mu = 0) = 0$ ,  $\vec{k}_W \cdot \hat{B} = 0$ , and  $v_s = v_{\parallel}$ . However, the phase-space quantization method reveals two important generalizations:

(1) The  $\tilde{\mu}$  defined in Eq. 1 is generically not measured from the energy of the bulk Weyl nodes. In particular, if we require that  $\mu$  is measured from the Weyl nodes, Eq. 1 should be modified by an offset  $\tilde{\mu} = \mu + \mu_0$ . This reconciles the quantum oscillations from phase-space quantization and energy-time quantization: the contribution from the area  $S_{k,0}$  enclosed by the Fermi arcs at  $\mu = 0$  is reflected in  $\mu_0$  while the contribution from the area change  $S_k - S_{k,0} = k_0^T \mu / v_s$  is reflected in  $\mu$ . For cases where the area  $S_{k,0}$  is large in comparison with the area change, the inclusion of  $\mu_0$  is necessary for the correct interpretation of the quantum oscillations.

It is natural that  $\mu_0$  should depend only on linearized Fermi-surface properties such as the area enclosed and the Fermi velocity, as the quantum oscillations generically encode only these low-energy universal features. We note that since  $v_s$  can in principle depend on chemical potential,  $\mu$ , so does  $\mu_0$  as defined above. For a quadratic surface dispersion,  $-\mu_0$  can be interpreted as the energy (relative to the bulk Weyl nodes) at which the surface arcs enclose zero area perpendicular to the magnetic field. More generally, as we show in Appendix B, the appropriate way to reconcile energy-time quantization is to set the zero of energy  $-\mu_0$  at  $\mu_0 = \frac{S_k}{\partial S_k / \partial \mu}$ , as the zero-area energy linearly extrapolated using the Fermi-surface property  $\frac{\partial S_k}{\partial \mu} \approx \frac{k_0^T}{v_s}$ .

(2) The thickness of the Weyl semimetal slab  $L_z$  contributes to the quantum oscillations through the phase offset of  $\phi(L_z) = (\vec{k}_W \cdot \hat{B} + \frac{2\mu}{v_{\parallel}}) L_z \sec \theta$ , which shifts the  $1/B$  positions of the quantum oscillation peaks. Comparing to Ref. 9, we see that the thickness dependent phase receives a contribution not only from the time  $t_{\text{bulk}} = \frac{L_z \sec \theta}{v_{\parallel}}$  taken to traverse the bulk via the chiral mode, but also from the momentum-space separation of the Weyl nodes projected onto  $\vec{B}$ . Interestingly, for fixed chemical potential  $\mu$ , there exists a special cone of angles of  $\vec{B}$ , defined by:  $\vec{k}_W \cdot \hat{B} = -\frac{2\mu}{v_{\parallel}}$ , for which the phase vanishes,  $\phi(L_z) = 0$ , for all  $L_z$ , such that the oscillations become independent of sample thickness.

**Numerical results and lattice model of Weyl semimetals** – To verify the semiclassical predictions from the phase-space quantization approach we study a simple lattice model of Weyl semimetal following the layered prescription in Ref. 4 and numerically calculate the density of states  $\rho(\mu, \vec{B})$  in a slab geometry. In the absence of the magnetic field, the Weyl semimetal is characterized by the following Hamiltonian:

$$H_{\vec{k}} = \sum_{z=1}^{L_z} (-1)^{z-1} \varepsilon_{\vec{k}} c_{\vec{k},z}^{\dagger} c_{\vec{k},z} + \sum_{z=1}^{L_z-1} h_{\vec{k},z} c_{\vec{k},z+1}^{\dagger} c_{\vec{k},z} + \text{H.c.} \quad (7)$$

where  $\vec{k} = (k_x, k_y)$  and the total number of layers  $L_z$  is odd so that the Fermi arcs on the top and bottom surfaces can be different<sup>4</sup>. We consider an in-plane dispersion  $\varepsilon_{\vec{k}} = -2 \cos k_x - 2 \cos k_y + \varepsilon_0$  that represents nearest-neighbor hopping of amplitude  $-1$  and an on-site energy of  $\varepsilon_0$ .  $h_{\vec{k},z}$  represents nearest-neighbor interlayer hopping with  $h_{\vec{k},z} = -t \sin k_y - t_0$  if  $z$  is odd and  $h_{\vec{k},z} = t \lambda \sin k_y + t_0$  if  $z$  is even. We choose  $\lambda > 1$ , which ensures  $h_{\vec{k},2} > h_{\vec{k},1}$  if  $k_y > 0$  and vice versa. This model generates two Weyl nodes at  $(\pm k_x^0, 0, 0)$  where  $k_x^0$  is the in-plane Fermi wave vector of  $\varepsilon_{\vec{k}}$  along the  $\hat{x}$  direction. By definition  $\vec{k}_W = 2k_x^0 \hat{x}$ . The surface Fermi arcs and the bulk chiral modes following the Weyl nodes are schematically consistent with the geometry in Fig. 1.

In the presence of a magnetic field  $\vec{B}$ , the translation symmetry in the  $\hat{y}$  direction is preserved in the Landau gauge  $\vec{A} = (0, \Phi_z x - \Phi_y z, -\Phi_y x)$ , where  $\Phi_i$  is the flux per plaquette perpendicular to the  $\hat{i}$  direction in units of the magnetic flux quantum magnetic flux quantum,  $\Phi_0 = \frac{h}{e}$ ,  $i = x, y, z$ . The Hamiltonian becomes:

$$\begin{aligned} H_{k_y} &= \sum_{x,z} h_{\pi_y(x,z+1/2),z} \left( e^{-i\Phi_y x} c_{x,z+1}^{\dagger} c_{x,z} + \text{h.c.} \right) \\ &- (-1)^z \left[ (\varepsilon_0 - 2 \cos \pi_y(x,z)) c_{x,z}^{\dagger} c_{x,z} - c_{x\pm 1,z}^{\dagger} c_{x,z} \right] \end{aligned} \quad (8)$$

where  $\pi_y(x,z) = k_y - A_y(x,z)$ .

The properties of this Hamiltonian such as the density of states  $\rho(\mu) = -\frac{1}{\pi L_x L_z} \sum_{x,z} \text{Im} G(x,z;x,z;\mu)$  at the chemical potential  $\mu$  can be calculated with the recursive Green's function method where the real space degrees of freedom in the  $\hat{x}$  direction are treated recursively<sup>13-15</sup>. For an incommensurate flux  $\Phi$ , physical properties of  $H_{k_y}$  between different choices of  $k_y$  are equivalent in the thermodynamic limit<sup>14,15</sup> and the summation over  $k_y$  can be neglected.

We choose parameters  $\varepsilon_0 = 3.0$ ,  $t = 1.0$ ,  $t_0 = 2.0$ ,  $\lambda = 2.0$ , and a small imaginary part  $\delta = 0.001$  in addition to the chemical potential  $\mu$  as the level broadening. In this model, although the chemical potential is at the Weyl nodes, the Fermi arcs enclose a  $k$ -space area of 8.515% of the surface Brillouin zone. We first consider a magnetic field purely in the  $\hat{z}$  direction. Eq. 1 would predict no quantum oscillations if one assumed  $\tilde{\mu} = 0$ , while Eq. 5 predicts quantum oscillations with a period

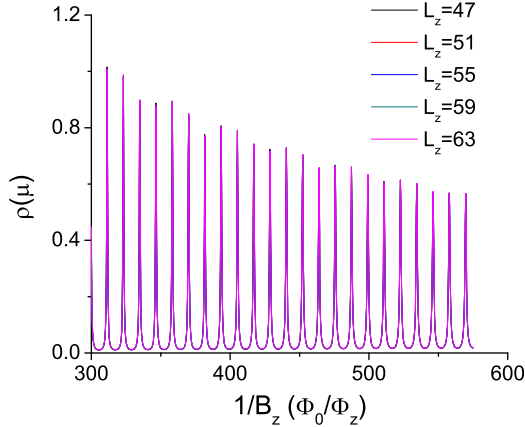


FIG. 2: The density of states  $\rho(\mu)$  versus the inverse magnetic field  $1/B_z$  (in unit of  $\Phi_0/\Phi_z$ ) for a Weyl semimetal slab of various thickness  $L_z$  shows clear quantum oscillations. The chemical potential  $\mu = 0$  is at the Weyl nodes. The characteristic quantum oscillation period is  $\Delta(\Phi_0/\Phi_z) = 11.74$ .

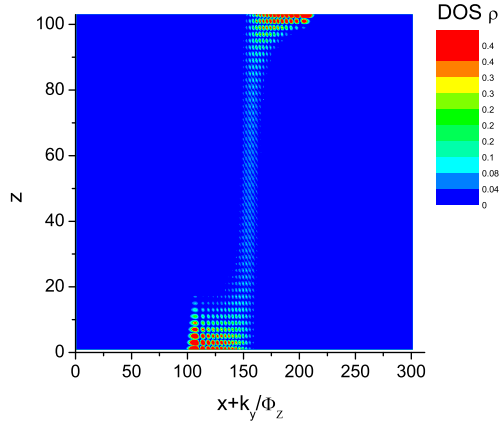


FIG. 3: The local density of states distribution in the  $x-z$  plane at  $\Phi_0/\Phi_z = 311.40$ ,  $\mu = 0$  and  $L_z = 103$  is consistent with the cyclotron orbit illustrated in Fig. 1 and clearly consists of components from the Fermi arcs on both Fermi surfaces and chiral LL modes in the bulk.

$\Delta(\Phi_0/\Phi_z) = 11.74$ . The numerical results of the density of states  $\rho(\mu)$  versus the inverse magnetic field  $1/B$  and various slab thickness  $L_z$ , shown in Fig. 2, show clear signatures of quantum oscillations whose period is in quantitative agreement with our formula.

To verify that the semiclassical orbit contains components in the bulk as well as on both of the top and bottom surfaces, we calculate the local density of states distribution  $\rho(x, z, \mu) = -\frac{1}{\pi} \text{Im} G(x, z; x, z; \mu)$  in the  $x-z$  plane with the  $x$  coordinate replaced by  $x + k_y/\Phi_z$ . The result for  $\Phi_0/\Phi_z = 311.40$ ,  $\mu = 0$  and  $L_z = 103$  is shown in Fig. 3. The Fermi arcs are at  $k_y > 0$  and  $k_y < 0$  for the top and bottom surfaces as well as the chiral modes in the

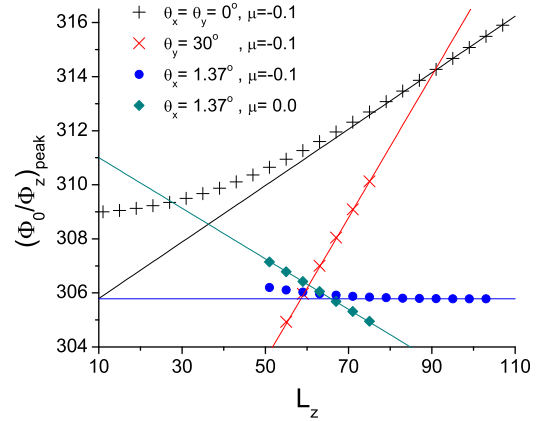


FIG. 4: Symbols mark the location of one of the density of states peaks as a function of the slab thickness  $L_z$  at different chemical potential  $\mu$  and magnetic field tilting angle  $\theta_y$  or  $\theta_x$ . The lines are the asymptotic expression in the large  $L_z$  limit derived from the positions of and the Fermi velocity around the Weyl nodes in the bulk:  $\left(\frac{\Phi_0}{\Phi_z}\right)_{\text{peak}} = \text{const.} + L_z \cdot \frac{-\mu}{2\pi t_0} \cdot \Delta\left(\frac{\Phi_0}{\Phi_z}\right)$  for a magnetic field in the  $\hat{z}$  direction, and refer to Appendix C for the expressions in the presence of a tilted magnetic field. While the peak positions typically show strong  $L_z$  dependence, notably, for particular ‘magic’ angles (blue circles), the peak positions asymptotically become nearly independent of sample thickness.

bulk are clearly visible.

In addition, Eq. 5 suggests that the thickness of the slab  $L_z$  changes the phase of the quantum oscillations, and thus the actual locations of the  $\rho(\mu)$  peaks in  $\Phi_0/\Phi_z$ . For a magnetic field in the  $\hat{z}$  direction and  $\mu = 0$ ,  $\vec{k}_W \cdot \vec{B} = 0$ , we expect no  $L_z$  dependence, which is confirmed in Fig. 2. For a finite  $\mu$  and a field in the  $\hat{z}$  direction, however, the shift  $\delta(1/B)$  of the peak positions is given by

$$\delta\left(\frac{\Phi_0}{\Phi_z}\right) = -\frac{\mu}{v_z} \frac{2\delta L_z}{2\pi} \cdot \Delta\left(\frac{\Phi_0}{\Phi_z}\right) = -\delta L_z \cdot \frac{\mu}{2\pi t_0} \cdot \Delta\left(\frac{\Phi_0}{\Phi_z}\right) \quad (9)$$

where  $\Delta\left(\frac{\Phi_0}{\Phi_z}\right)$  is the period of the quantum oscillations. We numerically observe this shift in the locations of the quantum oscillation peaks at  $\mu = -0.1$  in Fig. 4, where the location of one of the peaks is tracked as  $L_z$  is varied. The deviation from Eq. 9 at small  $L_z$  is due to the finite extent of the edge states (Fig. 3). At relatively large  $L_z$  where the physics in the center of the slab can be approximately treated as in the bulk, Eq. 9 gives an accurate description of the  $L_z$  dependence of the quantum oscillation phenomena. The above conclusions also hold true for a magnetic field that is tilted in the  $\hat{y}$  direction, e.g.  $\vec{B} = B_z(\hat{z} + \hat{y} \tan \theta_y)$ , where only the  $L_z$  coefficient is modified, see Fig. 4.

In comparison, the magnetic field tilted in the  $\hat{x}$  direction gives qualitatively different behavior, since  $\vec{k}_W \cdot \vec{B} \neq$



0 along  $\vec{B} = B_z(\hat{z} + \hat{x} \tan \theta_x)$ . First, there exists  $L_z$  dependence  $\delta\left(\frac{\Phi_0}{\Phi_z}\right) = -\delta L_z \cdot k_x^0 \tan \theta_x \cdot \Delta\left(\frac{\Phi_0}{\Phi_z}\right)/\pi$  for chemical potential  $\mu = 0$  at the energy of the Weyl nodes. Interestingly, for a given chemical potential  $\mu$ , such  $L_z$  dependence vanishes at a special tilting angle  $\theta_x^{(0)}$ , which satisfies

$$\tan \theta_x^{(0)} = -\frac{\mu}{t_0} \left[ 4(k_x^0)^2 - \mu^2 / \sin^2(k_x^0) \right]^{-1/2} \quad (10)$$

Numerical results for  $\mu = 0$  and  $\mu = -0.1$  confirm these expectations at tilting angle  $\theta_x^{(0)} \approx 0.024$  as in Eq. 10 for  $\mu = -0.1$  (Fig. 4). Derivations and further discussion on the  $L_z$  dependence of the peak positions in a tilted magnetic field  $\vec{B}$  are in Appendix C.

**Experimental consequences** – The new features revealed by the phase-space quantization treatment have several implications for experiments. As an example, the angle and thickness dependence of  $\phi(L_z)$ , observable by tracking individual quantum oscillation peaks as a function of field orientation, can be used to quantitatively determine the  $k$ -space separation of the Weyl nodes from quantum oscillation measurements, which can be challenging to accurately extract from other probes such as photoemission.

Moreover, the existence of a special set of angles for which the quantum oscillations become independent of sample thickness enables the following test: In recent experiments<sup>10</sup>, Moll et al. observed surface state oscillations in the Dirac semimetal  $\text{Cd}_3\text{As}_2$  in thin film devices with parallel surfaces, which were absent in triangular devices with non-parallel top and bottom surfaces. The absence of oscillations in the latter triangular samples can be attributed to the destructive interference of orbits with different  $L_z$ , due to the variation of device thickness along the triangle. The above computations predict that this geometric interference effect would be quenched for fields along the set of angles for which  $\phi(L_z) = 0$ , resulting in a reemergence of quantum oscillations. In contrast to the negative signature of not observing quantum oscillations in a triangular device, which could potentially arise from other extrinsic effects, such an observation would provide a clear positive signature of the non-local nature of the Weyl orbits. We note that observing this effect requires the field angle to be controlled to angular precision  $\delta\theta \lesssim 1/k_W L_z$ , which may require thin devices.

As a final application, the phase-space quantization formulation above naturally reveals the effect of bulk disorder on dephasing the quantum oscillations associated with Weyl orbits (see Appendix D for a detailed discussion of disorder effects). For conventional magnetic orbits, any scattering from impurities strongly suppresses quantum oscillations, requiring  $B \gg k_F/\ell_Q$  where  $\ell_Q$  is the quantum mean-free path (distinct from the transport mean-free path,  $\ell_{tr}$ , which only includes large-momentum transfer scattering) and  $k_F$  is the Fermi wave vector. As the surface-arc portion of the Weyl orbits is locally identical to conventional cyclotron motion, ob-

serving oscillations in the presence of disorder requires:  $B \gg k_0^T/\ell_Q$ . Naively, phase coherence along the bulk part similarly requires samples thinner than the quantum mean-free path,  $L_z \ll \ell_Q$ , a potentially stringent condition since while typical Weyl materials have large  $\ell_{tr}$ ,  $\ell_Q$  is typically much shorter<sup>16</sup>. However, the chiral nature of the bulk orbit along with the spatially correlated nature of disorder in low-density semimetals makes the bulk portion of the orbit more resilient to disorder effects.

Namely, for an electron traveling along a bulk chiral LL, a random potential  $V(\vec{r})$ , produces a local shift in the wave vector:  $\delta k_{\parallel}(\vec{r}) = -\tilde{V}(\vec{r}_{\perp}, z)/v_{\parallel}$ , where  $\tilde{V}$  is the matrix element of the disorder potential in the chiral mode localized within  $\approx \ell_B$  of transverse position  $\vec{r}_{\perp}$  in the  $xy$ -plane. The total phase accumulated in this fashion is given by:  $\delta\phi = \int_0^{L_z} dz \left( \delta k_{\parallel}(\vec{r}_{\perp}, z) - \delta k_{\parallel}(\vec{r}_{\perp} + \vec{d}, z) \right)$ , where the first term represents the random phase acquired traveling from bottom to top surface along the + chiral mode, and the second represents that of the return journey on the counter-propagating chiral mode of the opposite Weyl node. Between these two bulk legs of the orbit, the electron travels a spatial distance  $d \approx k_0^T \ell_B^2$  as it slides along the top surface Fermi arc. The typical disorder for low-density Weyl semimetals is poorly screened Coulomb impurities, which produce a potential that is spatially correlated over characteristic length scale  $\xi \approx \sqrt{\frac{\ell_{tr}}{\ell_Q} k_F^{-1}} \gg k_F^{-1}$ . For low-field,  $d \gg \xi$ , the two bulk legs of the orbit sample uncorrelated  $V$ , and dephasing indeed kills the quantum oscillations for  $L_z > \ell_B$ . However, for higher fields  $eB \gg k_0^T/\xi$ ,  $d \ll \xi$  and the top-to-bottom and bottom-to-top legs accumulate nearly canceling random phases, which leads to the much weaker requirement on sample thickness,  $L_z < \left(\frac{\xi}{d}\right)^2 \ell_Q \gg \ell_Q$ . For example, in  $\text{Cd}_3\text{As}_2$ , we estimate that the high-field regime is obtained for relatively low fields on the order of a few Tesla, in reasonable agreement with the observed field-scale at which surface-state oscillations onset in recent experiments<sup>10</sup>.

**Discussion** – In conclusion, we have compared quantum oscillations with respect to the inverse magnetic field  $1/B$  or chemical potential  $\mu$ . The accurate definition of chemical potential and its reference point is vital for correctly converting between and reconciling different semiclassical quantization perspectives. For the quantum oscillations from the surface Fermi arcs and bulk chiral modes in Weyl semimetals, the general reference point of  $\mu$  does not necessarily coincide with the Weyl points in the bulk. We derived the quantum oscillations using phase-space quantization conditions and proposed essential generalizations to previous conclusions and experimental consequences for generic Weyl semimetals. We also verified our claims numerically following the layered prescription.

We acknowledge insightful discussions with Itamar Kimchi, and Steven A. Kivelson. YZ was supported

by the NSF under Grant No. DMR-1265593. DB was supported by the NSF under Grant No. DGE-114747. PH was supported by the David and Lucile Packard Foundation. AP was supported by the Gordon

and Betty Moore Foundations EPiQS Initiative through Grant GBMF4307. AV was supported by ARO MURI program W911NF-12-1-0461.

- 
- <sup>1</sup> Xiangang Wan, Ari M. Turner, Ashvin Vishwanath, and Sergey Y. Savrasov, Phys. Rev. B 83, 205101 (2011).  
<sup>2</sup> Ari M. Turner, and Ashvin Vishwanath, arXiv-eprint:1301.0330 (2013).  
<sup>3</sup> F.D.M. Haldane, arXiv-eprint:1401.0529 (2014).  
<sup>4</sup> Pavan Hosur, Phys. Rev. B 86, 195102 (2012).  
<sup>5</sup> Su-Yang Xu, et al., Science, 349, 613 (2015).  
<sup>6</sup> B. Q. Lv, et al., Phys. Rev. X 5, 031013 (2015).  
<sup>7</sup> Hongming Weng, Chen Fang, Zhong Fang, B. Andrei Bernevig, and Xi Dai, Physical Review X 5, 011029 (2015); Shin-Ming Huang, Su-Yang Xu, et al., Nature Communications 6, 7373 (2015).  
<sup>8</sup> H.B. Nielsen, Masao Ninomiya, Physics Letters 130B, 6, 389 (1983).  
<sup>9</sup> Andrew C. Potter, Itamar Kimchi, Ashvin Vishwanath, Nature Communications 5, 5161(2014).  
<sup>10</sup> Philip J.W. Moll, Nityan L. Nair, Tony Helm, Andrew C. Potter, Itamar Kimchi, Ashvin Vishwanath, James G. Analytis, arXiv-eprint:1505.02817 (2015).  
<sup>11</sup> Yuval Baum, Erez Berg, S. A. Parameswaran, Ady Stern, arXiv-eprint:1508.03047 (2015).  
<sup>12</sup> L. Onsager, Phil. Mag. 43, 1006 (1952); I.M. Lifshitz and A.M. Kosevich, Sov. Phys. JETP 2, 636 (1956).  
<sup>13</sup> Alexander Croy, Rudolf A. Roemer, Michael Schreiber, Lecture Notes in Computational Science and Engineering, Springer, Berlin, 203(2006).  
<sup>14</sup> Yi Zhang, Akash V. Maharaj, Steven A. Kivelson, Physical Review B, 91, 085105 (2015).  
<sup>15</sup> Yi Zhang, Danny Bulmash, Akash V. Maharaj, Chao-Ming Jian, and Steven A. Kivelson, eprint-arXiv:1504.05205.  
<sup>16</sup> Tian Liang, Quinn Gibson, Mazhar N. Ali, Minhao Liu, R. J. Cava, and N. P. Ong, Nature Materials 14, 280 (2015).  
<sup>17</sup> There may exist additional phase contributions at the turning points connecting the surface and bulk orbits, which are presumably constant for large enough  $L_z$  and can be absorbed into the constant  $\gamma$ .

## Appendix A: Path integral derivation of energy-time quantization

Suppose that we have a quantum system with Hamiltonian  $H$  and corresponding classical action  $S$ . Let the eigenstates of  $H$  be  $|E\rangle$ . Then the propagator  $U(x, x'; t)$  obeys

$$U(x, x'; T) = \sum_E |\langle x|E\rangle|^2 e^{-iET} \quad (\text{A1})$$

Computing the propagator in the path integral instead, we can make a semiclassical approximation and assume that the only paths which contribute are those paths  $x_{cl}(t)$  which start at  $x$  and return there in time  $T$  according to the classical equations of motion. In this approx-

imation, we get an alternative expression for the same function:

$$U(x, x; T) \approx \mathcal{N} \sum_{x_{cl}(t)} e^{iS[x_{cl}(t)]} \quad (\text{A2})$$

where  $\mathcal{N}$  is a prefactor irrelevant to us.

Now come the main assumptions. Inspired by the free particle in a magnetic field, for which these assumptions definitely hold, assume that there are no nonstationary closed classical paths except when  $T = nT_0$  where  $T_0$  is some classical period. Furthermore, we assume that each classical path at  $T = nT_0$  is just  $n$  loops of a single closed orbit  $x_\alpha(t)$  which traverses the loop once in time  $T_0$ . In this case, absorbing any prefactors into  $\mathcal{N}$ ,

$$U(x, x; T) \approx \mathcal{N} \sum_\alpha \sum_n e^{inS[x_\alpha(t)]} \delta(T - nT_0) \quad (\text{A3})$$

$$= \mathcal{N} \sum_\alpha \int d\omega e^{-i\omega T} \sum_n e^{in(\omega T_0 + S[x_\alpha])} \quad (\text{A4})$$

$$= \mathcal{N} \sum_{\alpha, m} \int d\omega e^{-i\omega T} \delta(\omega T_0 + S[x_\alpha] - 2\pi m) \quad (\text{A5})$$

Comparing to the exact propagator Eq. A1, we see then that energies are labeled by  $m$  and  $\alpha$  and are given by

$$E_{m, \alpha} = \frac{2\pi m - S[x_\alpha]}{T_0} \quad (\text{A6})$$

This implies the energy-time quantization condition in Eq. 2, but also tells us more. Here  $S[x_\alpha]$  explicitly depends on the in-field Hamiltonian and thus the zero of energy for the Landau levels, so  $E_{m, \alpha}$  is automatically defined relative to the same zero. In particular, if we assume  $T_0 \sim 1/B$ , then in deriving a condition like Eq. 1 the energy  $\mu$  must be defined relative to the Landau level spectrum, which need not coincide with the natural zero of energy for the  $B = 0$  band structure.

## Appendix B: Quantum oscillations from energy-time quantization

In this appendix, we compare the quantum oscillations from the two different perspectives of energy-time quantization and phase-space quantization. The phase-space quantization gives the condition of the allowed semiclassical orbits:

$$\oint (\vec{k} - e\vec{A}) \cdot d\vec{r} = 2\pi(n + \gamma) \quad (\text{B1})$$

where the integral is over a constant energy contour in  $k$ -space at certain chemical potential  $\mu$ . With the semiclassical equations of motion, this can be re-written as:

$$\ell_B^2 S_k = \frac{\ell_B^2}{2} \oint k_{\perp} dk_{\parallel} = 2\pi(n + \gamma) \quad (\text{B2})$$

where  $k_{\perp}$  and  $k_{\parallel}$  are the wave vectors normal and parallel to the constant energy contour, respectively,  $S_k$  is the enclosed  $k$ -space area and  $\ell_B = 1/\sqrt{eB}$  is the magnetic length.

On the other hand, consider a dispersion  $\varepsilon(\vec{k})$  in two dimensions, the time needed to complete a cyclotron orbit at energy  $\varepsilon_n$  is

$$t = \ell_B^2 \oint \frac{dk_{\parallel}}{v_{\perp}(\vec{k})} \quad (\text{B3})$$

where  $v_{\perp}$  is the Fermi velocity perpendicular to the contour. The energy-time quantization states that  $(\varepsilon_n - \mu_0)t = 2\pi(n + \gamma)$ , which suggests:

$$\ell_B^2 \oint \frac{\varepsilon_n - \mu_0}{v_{\perp}(\vec{k})} dk_{\parallel} = 2\pi(n + \gamma) \quad (\text{B4})$$

where  $\mu_0$  is a constant offset and  $\gamma$  is a Berry phase contribution.

In particular, the two conditions in Eq. B2 and B4 match when

$$\frac{\varepsilon_n - \mu_0}{v_{\perp}} = \frac{k_{\perp}}{2} \quad (\text{B5})$$

For a parabolic dispersion, e.g., a two-dimensional electron gas  $\varepsilon_{\vec{k}} = k^2/2m$ , this is consistent with  $\mu_0 = 0$ . Namely, the zero of energy is at the bottom of the band.

For a more generic dispersion, we assume the Fermi velocity  $v_{\perp}$  is independent of  $\varepsilon_n$  in a small range around the chemical potential  $\varepsilon_F$ , then it is straightforward to take a derivative with respect to  $n$  and get:

$$\begin{aligned} \mu_0 \frac{d}{dn} \oint \frac{dk_{\parallel}}{v_{\perp}(\vec{k})} &= \frac{d}{2dn} \oint \frac{dk_{\parallel}}{v_{\perp}(\vec{k})} = \frac{dS_k}{dn} \\ \mu_0 &= S_k / \oint \frac{dk_{\parallel}}{v_{\perp}(\vec{k})} = S_k \cdot \frac{d\mu}{dS_k} \end{aligned} \quad (\text{B6})$$

Physically, given the Fermi surface area  $S_k$  and its derivative  $\frac{dS_k}{d\mu}$  with respect to the chemical potential  $\mu$  near the Fermi level, the linear extrapolation to lower energies gives the zero of energy as where the cross-section

area of the constant energy contour vanishes. For a linear dispersion  $\varepsilon = \pm v \left| \vec{k} \right|$  at chemical potential  $\varepsilon_F = vk_F$ , for example, the zero of energy is not at the Dirac node. It is straightforward to show that the consistent quantum oscillations are derived from energy-time quantization with  $\mu_0 = \varepsilon_F/2 = vk_F/2$ .

Therefore, it is vital to understand where is the zero of energy that the chemical potential  $\mu$  is measured from. As an example of the importance and ambiguity in correctly defining the zero of energy, the quantum oscillations of a two-dimensional electron gas  $\varepsilon_{\vec{k}} = k^2/2m$  is:

$$\frac{1}{B_n} = \frac{2\pi e}{S_k} \left( n + \frac{1}{2} \right) = \frac{2e}{k_F^2} \left( n + \frac{1}{2} \right) \quad (\text{B7})$$

where  $S_k = \pi k_F^2$  and  $k_F$  is the Fermi wave vector.

The energy-time quantization leads to the Landau levels:

$$\varepsilon_n = \omega_c (n + \gamma) - \mu_0 \quad (\text{B8})$$

where  $\omega_c = \frac{eB}{m}$  is the cyclotron frequency, and  $\mu_0$  and  $\gamma$  are unknown constants since  $\Delta\varepsilon \times t = 2\pi$  only gives the quantized level spacings  $\Delta\varepsilon = \varepsilon_n - \varepsilon_{n-1}$  and contains no information on the exact zero of energy. For the quantum oscillations at a fixed chemical potential  $\mu = k_F^2/2m$ , set  $\varepsilon_n = \mu$ :

$$\begin{aligned} \frac{k_F^2}{2m} &= \frac{eB_n}{m} (n + \gamma) - \mu_0 \\ \frac{1}{B_n} &= \frac{2e}{k_F^2 + 2m\mu_0} (n + \gamma) \end{aligned} \quad (\text{B9})$$

identical to Eq. B7 if we set  $\gamma = 1/2$  and  $\mu_0 = 0$  as we have derived above. Importantly, the fundamental behaviors of the quantum oscillations including its characteristic frequency are not consistently recovered by this formula if  $\mu_0 \neq 0$ .

### Appendix C: Thickness dependence in a tilted magnetic field

We can linearize the dispersion near the Weyl nodes for the lattice model we consider in the main text:

$$\varepsilon_{\vec{k}}^{\pm} = \left[ (2t_0 k_z)^2 + ((\lambda - 1)tk_y)^2 + (\pm 2 \sin k_x^0 k_x)^2 \right]^{1/2} \quad (\text{C1})$$

where  $k_x^0 = \cos^{-1}(\varepsilon_0/2 - 1)$  and the  $\pm$  signs are for the two Weyl nodes with opposite chirality.

---

For a magnetic field tilted in the  $\hat{y}$  direction  $\vec{B} = B_z (\hat{z} + \hat{y} \tan \theta_y)$ , the Fermi wave vector of the chiral modes are

$$\vec{k}_{\parallel,1(2)} = \pm \frac{\mu}{2(\lambda - 1)tt_0} \frac{4t_0^2 \tan \theta_y \hat{y} + (\lambda - 1)^2 t^2 \hat{z}}{\left[ 4t_0^2 \tan^2 \theta_y + (\lambda - 1)^2 t^2 \right]^{1/2}} \quad (\text{C2})$$

The shift of the peak positions is

$$\delta \left( \frac{\Phi_0}{\Phi_z} \right) = -\frac{\mu \cdot \delta L_z}{2\pi(\lambda-1)tt_0} \left[ 4t_0^2 \tan^2 \theta_y + (\lambda-1)^2 t^2 \right]^{1/2} \Delta \left( \frac{\Phi_0}{\Phi_z} \right) \quad (\text{C3})$$

Similarly, for a magnetic field tilted in the  $\hat{x}$  direction  $\vec{B} = B_z(\hat{z} + \hat{x} \tan \theta_x)$ , the Fermi wave vector of the chiral modes are

$$\vec{k}_{\parallel,1(2)} = \pm \frac{\mu}{2t_0 \sin k_x^0} \frac{t_0^2 \tan \theta_x \hat{x} + \sin^2 k_x^0 \hat{z}}{[t_0^2 \tan^2 \theta_x + \sin^2 k_x^0 t^2]^{1/2}} \quad (\text{C4})$$

together with the location of the Weyl nodes at  $(\pm k_x^0, 0, 0)$  therefore  $\vec{k}_W = 2k_x^0 \hat{x}$ , the shift of the peak positions is

$$\delta \left( \frac{\Phi_0}{\Phi_z} \right) = - \left[ \frac{\mu}{2t_0 \sin k_x^0} (t_0^2 \tan^2 \theta_x + \sin^2 k_x^0)^{1/2} + k_x^0 \tan \theta_x \right] \frac{2\delta L_z}{2\pi} \cdot \Delta \left( \frac{\Phi_0}{\Phi_z} \right)$$

There exists a residual  $L_z$  dependence  $\delta \left( \frac{\Phi_0}{\Phi_z} \right) = -\delta L_z \cdot k_x^0 \tan \theta_x \cdot \Delta \left( \frac{\Phi_0}{\Phi_z} \right) / \pi$  at  $\mu = 0$ . In addition, at tilting angle  $\theta_x^{(0)}$  satisfying

$$\tan \theta_x^{(0)} = -\frac{\mu}{t_0} \left[ 4(k_x^0)^2 - \mu^2 / \sin^2(k_x^0) \right]^{-1/2} \quad (\text{C5})$$

the coefficient in the square bracket vanishes, and the quantum oscillations have no manifest  $L_z$  dependence.

---

$\vec{k}'$  by a factor of  $(1 - \cos \theta_{\vec{k}, \vec{k}'}) \approx \left( \frac{1}{k_F \xi} \right)^2$ , where  $\theta_{\vec{k}, \vec{k}'}$  is the angle between  $\vec{k}, \vec{k}'$ , is given by:

$$\tau_{\text{tr}}^{-1} = \frac{1}{(k_F \xi)^2} \tau_Q^{-1} \quad (\text{D2})$$

We can determine the parameter  $V_0^2$  in terms of the measurable quantities  $\tau_Q^{-1}$ :

$$V_0^2 = \frac{\pi v_F \xi^2}{\tau_Q} \quad (\text{D3})$$

## Appendix D: Disorder Effects

### 1. Disorder Model

As a model for the bulk effects of disorder, consider Weyl nodes with linear dispersion, and a random potential  $V(r)$  with Gaussian distribution characterized by correlations  $\overline{V(r)V(r')} = V_0^2 f^{(3)}(r-r')$ , where  $f^{(d)}(r)$  is a smooth function that decays with characteristic length scale  $\xi$ , which, for concreteness, we will take as a normalized  $d$ -dimensional Gaussian with variance  $\xi^2$ , and  $\overline{(\dots)}$  indicates an average over disorder configurations.

In the Born approximation, the quantum lifetime,  $\tau_Q$ , characterizing the timescale between elastic scattering events in the bulk in the absence of a field is:

$$\tau_Q^{-1} = \frac{2\pi\nu(0)V_0^2}{(k_F\xi)^2} \quad (\text{D1})$$

which is related to the quantum mean-free path by  $\ell_Q = \frac{\tau_Q}{v}$ , where  $v_F$  is the geometric average of the different spatial components of the bulk velocity. Here  $\nu(0) = \frac{k_F^2}{2\pi^2 v_F}$  is the density of states for the Fermi-surface of a single Weyl node, and  $k_F = \frac{\mu}{v_F}$  is the Fermi wave vector for the Weyl pocket.

In contrast, the transport lifetime obtained by weighting scattering events between states with momenta  $\vec{k}$  and

### 2. Different Scattering Processes

For the bulk portion of the Weyl orbit, there are three potentially detrimental sources of disorder induced dephasing: 1) intervalley scattering between opposite chirality Weyl nodes, 2) scattering between different Landau levels (LLs) within a single Weyl node, and 3) random phase accumulated along the chiral LLs in the absence of inter-LL scattering. We will consider each of these channels in turn. The rates for these dephasing channels add, indicating that their inverse length scales add:  $\ell_{\text{tot}} = \left( \sum_i \frac{1}{\ell_i} \right)^{-1}$ , indicating that the sample thickness limitation on observing quantum oscillations will be set by the shortest scattering length scale.

### 3. Intervalley Scattering

As intervalley scattering requires momentum transfer  $\approx k_W$ , for long-wavelength disorder, intervalley scattering will be suppressed by  $\frac{1}{(k_W \xi)^2}$  compared to total quantum scattering, indicating:

$$\ell_{\text{inter-valley}} \approx (k_W \xi)^2 \ell_Q \quad (\text{D4})$$

In particular, since  $k_W > k_F$ , this length scale is even longer than the transport mean free path,  $\ell_{\text{tr}} \approx (k_F \xi)^2 \ell_Q$ , for all field strengths.



#### 4. Inter Landau level Scattering

For  $\mu$  larger than the LL spacing, multiple non-chiral bulk LLs will coexist at the same energy as the chiral modes, and scattering between chiral and non-chiral modes within the same Weyl node is possible. However, since the wavefunctions of different LL modes differ on lengthscales of order  $\ell_B$ , for  $\xi \gg \ell_B$ , the matrix element for inter-LL scattering between levels with indices  $m$  and  $n$  is suppressed by approximately a factor of  $\left(\frac{\ell_B}{\xi}\right)^{|m-n|}$ :

$$\begin{aligned} V_{n,m} &= \langle u_n | V | u_m \rangle \\ &\approx \int dx \frac{e^{-x^2/2\ell_B^2}}{2\pi\ell_B^2} \sum_r H_n(x) H_m(x) \frac{x^r V^{(r)}(0)}{r!} \\ &\approx \left(\frac{\ell_B}{\xi}\right)^{|m-n|} V_0 \end{aligned} \quad (\text{D5})$$

where  $H_n(x)$  is the  $n^{\text{th}}$  Hermite polynomial. The dominant mixing will hence come from minimal difference in LL indices, and hence, for  $\ell_B \ll \xi$ , the inter-LL scattering rate is suppressed by a factor of  $\frac{|V_{0,1}|^2}{|V_0|^2} \approx \left(\frac{\ell_B}{\xi}\right)^2$ , i.e. we expect:

$$\ell_{\text{inter-LL}} \approx \left(\frac{\xi}{\ell_B}\right)^2 \ell_Q \quad (\text{D6})$$

We will see below that this length scale is longer than that set by dephasing while propagating along the chiral bulk modes, which is expected to be the dominant limiting factor in observing quantum oscillations.

#### 5. Dephasing within the bulk chiral modes

In the previous section, we have seen that inter-LL scattering may be neglected for  $\ell_B \ll \xi$ , and  $L_z \ll \ell_{\text{inter-LL}}$ . In this regime, the bulk portion of the orbit occurs purely within the chiral modes of the lowest Landau level. In the presence of an impurity potential  $V(\vec{r})$  that varies smoothly on the length scale of  $k_F^{-1}$ , we can model the  $\pm$  chiral mode localized within  $\ell_B$  of the guiding center position  $\vec{r}_\perp$  in the  $xy$  plane, by the continuum Hamiltonian:

$$H_{ch}^{(\pm)}(\vec{r}_\perp) = \psi^\dagger (\mp i v_F \partial_z - U(\vec{r}_\perp, z)) \psi \quad (\text{D7})$$

where  $U(\vec{r}_\perp, z) = \int d^2 \delta r_\perp V(r_0 + \delta r_\perp, z) |u_0(r_\perp)|^2$  is the matrix element of  $V$  within the lowest LL orbital with guiding center coordinate  $\vec{r}_\perp$  which has wave function  $u_0(r_0 + \delta r_\perp) \sim \frac{1}{4\pi\ell_B^2} e^{-\delta r_\perp^2/(4\ell_B^2)}$ .

For moderate fields,  $\ell_B \ll \xi$ , the mean-square of these matrix elements is then given by:

$$\overline{U(r, z)U(r, z')} \approx \frac{V_0^2}{2\pi\xi^2} f^{(1)}(z - z') \quad (\text{D8})$$

The random phase factor accumulated through the bulk portion of the orbit (ignoring mixing between chiral and non-chiral levels) is:

$$e^{i\delta\phi} = \exp \left[ i \int_0^L \frac{U_{r_\perp}(z) - U_{r_\perp+d}(z)}{v_F} dz \right] \quad (\text{D9})$$

where the first term comes from propagating from bottom to top surface along the + chiral LL, and the second comes from returning from top to bottom surface along the counter-propagating - chiral LL. In between the electron travels spatial distance  $d = k_0^T \ell_B^2$  as it slides along the surface arc of the top surface.

Averaging the disorder phase over disorder gives:

$$\overline{e^{i\delta\phi}} = e^{-\frac{1}{2v_F^2} \int_0^L dz dz' \overline{U(r, z)U(r, z') - U(r+d, z)U(r+d, z')}} \quad (\text{D10})$$

The suppression factor depends strongly on the ratio of the orbit size,  $d = k_0^T \ell_B^2$ , to the disorder correlation length.

##### a. Low field regime ( $d \gg \xi$ )

In the low field regime,  $d \gg \xi$ ,  $U(r, z)$  is uncorrelated with  $U(r + k_0 \ell_B^2, z)$ , and:

$$\overline{e^{i\delta\phi}} \approx e^{-\frac{2}{v_F^2} \int_0^L dz dz' \overline{U(r, z)U(r, z')}} \approx e^{-\frac{v_F^2 V_0^2}{\pi \xi^2} L_z} \quad (\text{D11})$$

from which we identify the relevant bulk ‘‘mean-free path’’ length scale:

$$\ell_{ch} = \frac{\pi v_F^2 \xi^2}{V_0^2} = v_F \tau_Q = \ell_Q \quad (\text{D12})$$

which is just the quantum mean-free path.

##### b. High field regime ( $d \ll \xi$ )

On the other hand, for strong fields,  $d \ll \xi$ , the phase accumulated in traversing from bottom to top surfaces samples almost the same disorder configuration as the reverse trip, resulting in near cancellation of the total accumulated phase, and leading to a longer effective dephasing length for the chiral channel  $\ell_{ch} \gg \ell_Q$ .

To estimate  $\ell_{ch}$ , in this regime we also need the expression for:

$$\overline{U(r, z)U(r+d, z')} \approx \left[ 1 - \left(\frac{d}{\xi}\right)^2 \right] \overline{U(r, z)U(r, z')} \quad (\text{D13})$$

with which we find:

$$\begin{aligned} \overline{e^{i\delta\phi}} &\approx e^{-\frac{1}{v_F^2} \int_0^L dz dz' \overline{U(r, z)U(r, z') - U(r, z)U(r+k_0 \ell_B^2, z')}} \\ &\approx e^{-\left(\frac{d}{\xi}\right)^2 \frac{L_z}{\ell_Q}} \equiv e^{-L_z/\ell_{ch}} \end{aligned} \quad (\text{D14})$$

Hence, in the high-field regime, the chiral nature of the bulk LLs and long correlation length of disorder enables quantum oscillations to be observed for sample thicknesses up to

$$\ell_{ch} \approx \left(\frac{\xi}{d}\right)^2 \ell_Q \quad (\text{D15})$$

which can substantially exceed the quantum mean-free path.

We can express the enhancement of the dephasing length for the bulk chiral modes,  $\ell_{ch}$ , compared to the quantum mean-free path,  $\ell_Q$ , in terms of measurable quantities including: 1) the ratio  $\left(\frac{\tau_{tr}}{\tau_Q}\right)$  of transport to quantum lifetimes obtained respectively from transport

and bulk quantum oscillation measurements, and 2) the frequency of the surface oscillations  $f \approx k_F k_0$ , as:

$$\frac{\ell_{ch}}{\ell_Q} = \left(\frac{\xi}{d}\right)^2 \approx \frac{\sqrt{\tau_{tr}/\tau_Q}}{f/B} \quad (\text{D16})$$

We note that the “high-field” regime may be accessed for relatively modest field scales. For example, for  $\text{Cd}_3\text{As}_2$ ,  $k_F \xi \approx \sqrt{\frac{\tau_{tr}}{\tau_Q}} \approx 10-30$ ,<sup>16</sup> and  $f \approx 60T$ ,<sup>10</sup> and we estimate that  $d \gg \xi$  can be achieved for fields of order a few Tesla, which is incidentally consistent with the lowest fields for which surface oscillations are seen in recent thin film devices<sup>10</sup>.